J. Fluid Mech. (1990), *vol.* 210, *pp.* 353–370
Printed in Great Britain

Periodic flows through curved tubes: the effect of the frequency parameter

By COSTAS C. HAMAKIOTES AND STANLEY A. BERGER
Department of Mechanical Engineering, University of California, Berkeley, CA 94720, USA

(Received 21 October 1988)

In a previous paper we reported on the effect of Dean number, κ_m, on the fully developed region of periodic flows through curved tubes. In this paper we again consider a sinusoidally varying volumetric flow rate in a curved pipe of arbitrary curvature ratio, δ, and investigate the effect of frequency parameter α, and Reynolds number Re_m on the flow. Specifically, we report on the flow-field development for the range $7.5 \leqslant \alpha \leqslant 25$, and $50 \leqslant Re_m \leqslant 450$. The results, obtained by numerical integration of the full Navier–Stokes equations, reveal a number of characteristics of the flow previously unreported. For low values of Re_m the secondary flow consists of a single vortex (Dean-type motion) in the half-cross-section at all times and for all values of α studied. For higher Re_m we observe inward 'centrifuging' (Lyne-type motion) at the centre. This motion always occurs during the accelerating period of the volumetric flow rate. It appears at lower α for higher Re_m and, for the given Re_m at which it appears, it occurs at earlier times in the cycle for lower α. A striking feature is observed for $\alpha = 15$ for the range $315 \leqslant Re_m \leqslant 400$: period tripling. The flow field varies periodically with time for the duration of three volumetric-flow-rate cycles then repeats for the subsequent three cycles, and so on. The computed axial pressure gradient also varies periodically with time but with the same period as the volumetric flow rate.

1. Introduction

Curved-pipe flows were first studied by Dean (1927, 1928). Owing to their richness in physical phenomena and their occurrence in a wide spectrum of applications there exists now a large literature on such flows, both steady and unsteady. For a comprehensive review of flows through curved pipes the reader may consult Berger, Talbot & Yao (1983), Itō (1987) and Nandakumar & Masliyah (1986).

The motivation for the present work has been its physiological application, in particular to the flow of blood through the aortic arch. Studies, both theoretical and experimental, of flow in curved pipes have yielded much information helpful in understanding the flow in the aorta, for example that the flow in the aorta is normally laminar, in part, because curvature stabilizes the flow and, therefore, delays transition to turbulence. Nevertheless, many questions regarding the nature of the flow in the aorta and its implications still remain. Particularly interesting is whether there are regions in the aorta where curvature is likely to enhance the development of atherosclerotic plaques. In the recent past two competing theories have confronted each other with opposing evidence regarding the initiation of atherosclerosis (Caro, Fitz-Gerald & Schroter 1971; and Fry 1968, 1973). These theories have one feature in common – they relate the shear stress on the wall to the pathological cause of atherosclerosis. Caro *et al.* claim that deposits occur in areas of

low wall shear, the result of low mass diffusion of cholesterol away from the artery wall in which it is produced, while Fry suggests that they occur in areas of maximum wall shear, owing to mechanical damage to the vessel walls. (For an extensive review of the role of fluid mechanics in atherogenesis the reader is referred to Nerem 1981 and Schettler *et al.* 1983.) More recent studies (Friedman *et al.* 1981; Ku *et al.* 1985), which have compared measurements in in-vitro scale models of the human circulatory system with human physiological and anatomical data, have shown intimal plaque thickening to be greatest in regions of low, rather than high, shear stress. Moreover, these studies have shown that oscillations in the direction of the wall shear, such as occur in pulsatile flow, are correlated with enhanced plaque formation. These authors conclude that low mean shear stress and marked oscillations in the direction of wall shear stress may be critical factors in atherogenesis. (Although these studies were carried out in models of arterial bifurcations with straight parent and daughter vessels, the pulsatile flow created helical streamlines reminiscent of flows in curved tubes.)

In the current study we impose a volumetric flow rate of the form

$$Q^*(\omega t^*) = Q^*_{\mathrm{DC}} + Q^*_{\mathrm{AC}} \cos(\omega t^* + \pi).$$

The asterisk denotes dimensional quantities. When we non-dimensionalize using Q^*_{DC}, the flow rate takes the form

$$Q(t) = 1 + \gamma \cos(t + \pi). \tag{1.1}$$

We seek a flow field, in the fully developed region of the pipe, which is consistent with this volumetric flow rate. The 'fully developed' characterization is meant in the sense that the flow is periodic in time at any cross-section, and independent of axial position. Our problem, therefore, is two-dimensional, but all three velocity components are non-zero. Consequently, all three momentum equations need to be solved.

The fluid is assumed to be incompressible and Newtonian and the flow laminar.

2. Mathematical and numerical formulations

The mathematical formulation and the numerical procedures are the same as reported by Hamakiotes & Berger (1988), and therefore we omit them here. We limit ourselves to displaying the governing equations of motion in conservative, dimensionless form, for momentum and mass, in a toroidal coordinate system (figure 1):

$$St_{\mathrm{m}} \frac{\partial u}{\partial t} + \frac{1}{rB}\left[\frac{\partial}{\partial r}(rBu^2) + \frac{\partial}{\partial \phi}(Buv) - Bv^2 - \delta r w^2 \cos\phi\right] = -\frac{\partial P}{\partial r} + \frac{1}{Re_{\mathrm{m}}}\left\{\frac{1}{rB}\left[\frac{\partial}{\partial r}\left(rB\frac{\partial u}{\partial r}\right) + \frac{\partial}{\partial \phi}\left(\frac{B}{r}\frac{\partial u}{\partial \phi}\right)\right] - \frac{1}{r^2}\left(2\frac{\partial v}{\partial \phi} + u\right) + \frac{\delta v \sin\phi}{rB} + \frac{\delta^2 \cos\phi}{B^2}(v\sin\phi - u\cos\phi)\right\}, \tag{2.1}$$

$$St_{\mathrm{m}} \frac{\partial v}{\partial t} + \frac{1}{rB}\left[\frac{\partial}{\partial r}(rBuv) + \frac{\partial}{\partial \phi}(Bv^2) + Buv + \delta r w^2 \sin\phi\right] = -\frac{1}{r}\frac{\partial P}{\partial \phi} + \frac{1}{Re_{\mathrm{m}}}\left\{\frac{1}{rB}\left[\frac{\partial}{\partial r}\left(rB\frac{\partial v}{\partial r}\right) + \frac{\partial}{\partial \phi}\left(\frac{B}{r}\frac{\partial v}{\partial \phi}\right)\right] + \frac{1}{r^2}\left(2\frac{\partial u}{\partial \phi} - v\right) - \frac{\delta u \sin\phi}{rB} - \frac{\delta^2 \sin\phi}{B^2}(v\sin\phi - u\cos\phi)\right\}, \tag{2.2}$$

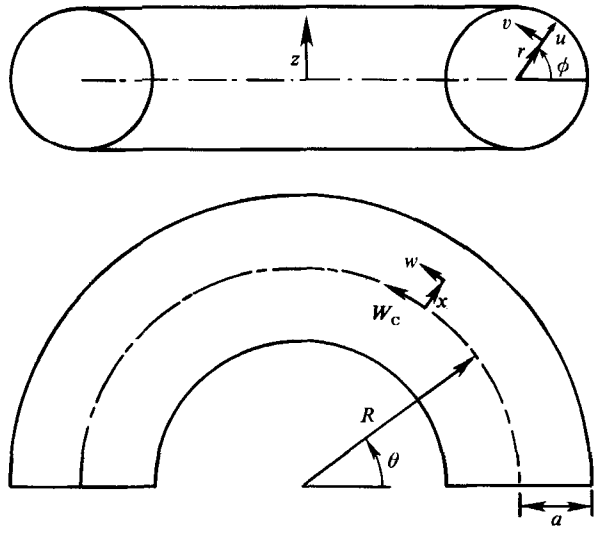

FIGURE 1. Toroidal coordinate system.

$$St_m \frac{\partial w}{\partial t} + \frac{1}{rB}\left[\frac{\partial}{\partial r}(rBuw) + \frac{\partial}{\partial \phi}(Bvw) + \delta rw\,(u\cos\phi - v\sin\phi)\right] = -\frac{\delta}{B}\frac{\partial P}{\partial \theta} + \frac{1}{Re_m}\left\{\frac{1}{rB}\left[\frac{\partial}{\partial r}\left(rB\frac{\partial w}{\partial r}\right) + \frac{\partial}{\partial \phi}\left(\frac{B}{r}\frac{\partial w}{\partial \phi}\right)\right] - \frac{w\delta^2}{B^2}\right\}, \quad (2.3)$$

$$\frac{\partial}{\partial r}(rBu) + \frac{\partial}{\partial \phi}(Bv) = 0, \quad (2.4)$$

where $\delta = a/R$ and $B = 1 + \delta r\cos\phi$. Re_m is the mean Reynolds number, defined as $Re_m = aW_m/\nu$; St_m is the mean Strouhal number, defined as $St_m = a\omega/W_m$; and α is the frequency parameter, defined as $\alpha = a(\omega/\nu)^{\frac{1}{2}}$, which is also equal to $(Re_m St_m)^{\frac{1}{2}}$.

The dimensionless variables appearing above have been defined as follows:

$$V = \frac{V^*}{W_m}, \quad P = \frac{P^*}{\rho W_m^2}, \quad r = \frac{r^*}{a}, \quad t = \omega t^*, \quad \tau = \frac{a\tau^*}{\mu W_m}, \quad (2.5)$$

where the asterisk indicates dimensional quantities, $\boldsymbol{r}$ is the position vector, μ is the coefficient of viscosity, ν is the kinematic viscosity, ρ is the density, $\boldsymbol{V}$ is the velocity vector, P is the pressure, t is the time, τ is the viscous-stress tensor and $W_m = Q^*_{DC}/\pi a^2$. The reference velocity W_m corresponds to the volumetric flow rate Q^*_{DC} pumped through a cross-sectional area πa^2, and can be alternatively viewed as the time-mean value of the axial velocity. Here, a is the radius of the pipe (figure 1).

Periodic flows through curved pipes are characterized by three parameters: the frequency parameter α, the amplitude ratio γ (see (1.1)), and the mean Dean number κ_m. Their physical interpretation is discussed in Lyne (1971) and in Hamakiotes & Berger (1988). The definitions of these and other parameters are listed in table 1.

The assumed boundary conditions are: no-slip at the wall; symmetry across the centreplane; fully developed flow.

To solve the system (2.1)–(2.4) we use Chorin's (1968) Projection Method. The numerical details and finite-difference discretization can be found in Hamakiotes & Berger (1988).

Name	Definition
Curvature ratio	$\delta = a/R$
Amplitude ratio	$\gamma = Q^*_{AC}/Q^*_{DC}$
Mean axial velocity	$W_m = Q^*_{DC}/\pi a^2$
Mean Strouhal number	$St_m = \dfrac{\omega a}{W_m}$
Mean Reynolds number	$Re_m = \dfrac{W_m a}{\nu}$
Mean Dean number	$\kappa_m = \dfrac{2W_m a}{\nu}\left(\dfrac{a}{R}\right)^{\frac{1}{2}} = 2Re_m \delta^{\frac{1}{2}}$
Secondary Reynolds number	$Re_s = \dfrac{W_m^2 a}{R\omega\nu} = \dfrac{Re_m}{St_m}\delta$
Frequency parameter	$\alpha = a(\omega/\nu)^{\frac{1}{2}} = (St_m Re_m)^{\frac{1}{2}}$

TABLE 1. Definitions of important parameters

3. Results and discussion

3.1. *Preliminaries*

To validate our code we first reproduced Gong's (1979) results. The results of our simulation are presented in Hamakiotes (1988). Excellent agreement is observed. Further, to test the consistency of the code we reproduced Gong's results using different meshes and different time steps. We experimented with 240 and 330 time steps in the cycle with very little or no change in the results. So most of our results were obtained with 240 time steps per cycle, except those for small α which required a larger number of time steps – typically 400. For the spatial discretization we used two non-uniform staggered meshes, 14×19 and 16×21, and three uniform staggered meshes, 19×19, 21×21 and 23×23, on the half-cross-section. From the 14×19 to the 21×21 mesh very little change was observed in the flow field. The differences were larger in the shear stress because derivatives accentuate errors. Between the 21×21 and 23×23 meshes the change in the shear stress was less than 1%, whereas more than a three-fold increase in time was required for the latter mesh compared to the former.

Upon convergence the divergence of the velocity was less than 10^{-6} and the numerically computed volumetric flow rate was calculated to be within less than 2×10^{-4}% of its analytic value. Owing to the iterative nature of our algorithm, integration of the equations must be carried out for a number of cycles until periodicity of the results is achieved. Typically, fifteen cycles were required for periodicity. A significant improvement in the rate of convergence occurred if the calculations started at the beginning, or shortly thereafter, of the accelerative part of the volumetric flow rate. Figure 2 shows the dimensionless volumetric flow rate. We started the calculations at the minimum of the flow rate. Another significant improvement was observed if we did not allow the minimum of the volumetric flow rate to ever become exactly zero. The number of cycles required for convergence was found to increase with increasing frequency parameter and Reynolds number.

In our simulations we used $\gamma = 0.98$ and $\delta = \frac{1}{7}$, although the equations, (2.1)–(2.4), and the numerical formulation we use are valid for any value of δ. We report here our results for the ranges $7.5 \leqslant \alpha \leqslant 25$ and $50 \leqslant Re_m \leqslant 450$. A complete list of all the

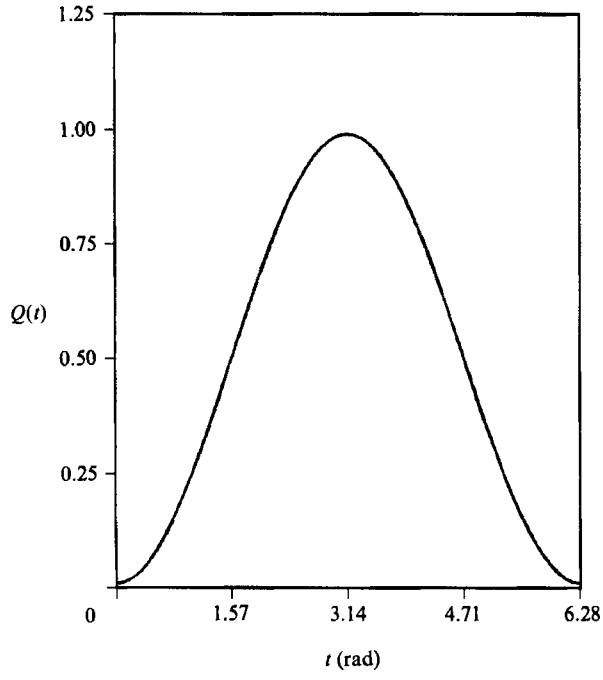

FIGURE 2. Volumetric flow rate: $Q = \frac{1}{2}[1+0.98\cos(t+\pi)]$.

parameter values studied is given in table 2. For reasons of economy of space we present only a small portion of these results.

We discuss the flow-field development for $Re_m = 375$ and $\alpha = 7.5$, 10 and 15. The results are shown in figures 3–13. Figure 3 shows for all the cases the numerically computed axial pressure gradient (with its algebraic sign) for the imposed volumetric flow rate of figure 2. If we take the algebraic sign into consideration we conclude that, consistent with previous investigations, the driving axial pressure gradient (i.e. the negative of part (*a*) of all figures) leads the volumetric flow rate by approximately 90°.

The six parts, (*a–f*), of figures 4, 6, 8, 10, and 12 exhibit the flow-field development at various times in the cycle. Owing to the assumed symmetry across the centreplane, on the upper half of the cross-section we have plotted the secondary-velocity vectors, and on the lower half the axial isovelocity contours. The inner bend is located at the left-hand side of each of these figures, and the outer bend at the right-hand side. To keep the secondary-velocity vectors reasonably sized and so that they do not extend beyond the cross-sectional boundary, they are multiplied by a scaling factor, λ, which in this case has the value 0.5. In each of these figures we have plotted a vector which extends from the centre outwards, rightward, along the centreline. A vector of length equal to this vector would correspond to a secondary velocity of magnitude λ, so in this case, for example, a vector of length equal to half the length of the radius of the pipe would have magnitude equal to 0.5. All figures refer to dimensionless quantities.

Figures 5, 7, 9, 11, and 13 show the circumferential and axial components of the shear stress for the different flow cases.

Re_m	κ_m	α	St_m	Re_s
50	37.796	7.50	1.1250	6.3492
50	37.796	10.0	2.0000	3.5714
50	37.796	15.0	4.5000	1.5873
50	37.796	20.0	8.0000	0.8929
150	113.39	7.50	0.3750	57.143
150	113.39	10.0	0.6667	32.143
150	113.39	15.0	1.5000	14.286
150	113.39	20.0	2.6667	8.0357
250	188.98	7.50	0.2250	158.73
250	188.98	10.0	0.4000	89.286
250	188.98	13.0	0.6760	52.832
250	188.98	15.0	0.9000	39.683
250	188.98	25.0	2.5000	14.286
300	226.78	7.50	0.1875	228.57
300	226.78	10.0	0.3333	128.57
300	226.78	15.0	0.7500	57.143
315	238.12	15.0*	0.7143	63.000
325	245.68	15.0*	0.6923	67.063
350	264.58	7.50	0.1607	311.11
350	264.58	10.0	0.2857	175.00
350	264.58	15.0*	0.6429	77.778
350	264.58	25.0	1.7857	28.000
375	283.47	7.50	0.1500	357.14
375	283.47	10.0	0.2667	200.89
375	283.47	15.0*	0.6000	89.286
400	302.37	10.0	0.2500	228.57
400	302.37	15.0*	0.5625	101.59
400	302.37	25.0	1.5625	36.570
450	340.17	10.0	0.2222	289.29

TABLE 2. Range of parameters investigated. $\delta = \frac{1}{7}$, $\gamma = 0.98$. * Indicates period tripling

3.2. *Flow-field and shear-stress development*

We start with the flow-field development over the cycle for $\alpha = 7.5$, $Re_m = 375$, and $\alpha = 10$, $Re_m = 375$. The results are shown in figures 3–7. Figure 3 shows the numerically computed axial pressure gradient necessary to sustain the volumetric flow rate of figure 2. As discussed in §3.1, this pressure gradient, and those which follow, are plotted with their algebraic sign. It is important to notice that all computed axial pressure gradients are periodic with time and have a phase difference of approximately 90° from the volumetric flow rate. Looking at the results presented here for $\alpha = 7.5$, 10, 15 and $Re_m = 375$ and at the remainder of the results we have obtained, we conclude that the amplitude of the axial pressure gradient decreases with increasing Reynolds number, as expected, but increases with increasing frequency parameter keeping Re_m constant.

Regions of reverse axial flow are observed at the beginning and end of the volumetric-flow-rate cycle, i.e. at the end of the decelerative part and at the beginning of the accelerative part of the cycle. Such regions are seen in parts (*e*) and (*f*) of all the figures. These figures show that when the extent of the reverse axial flow region is at its maximum, (part *f* of all the figures), it occupies the inner part of the cross-section. From part (*e*) of all the figures we can infer that such reversal of the flow is initiated at the very inner point of the cross-section. Part (*a*) of all the figures shows the end of reversed axial flow. At this point we have a region around the centre

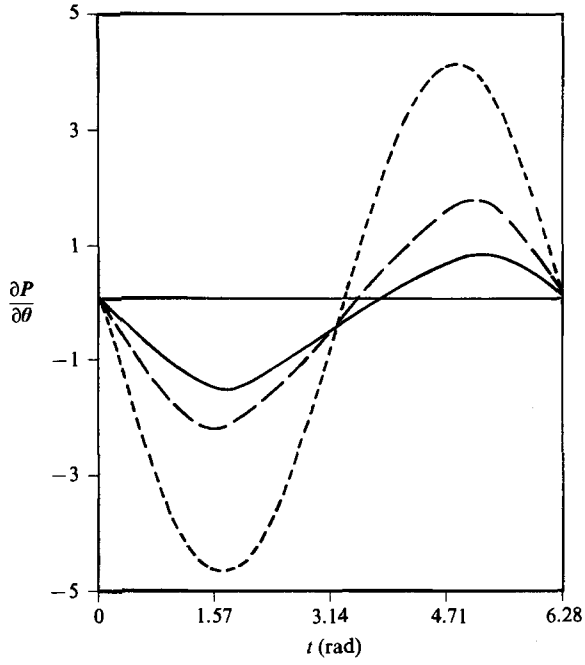

FIGURE 3. Calculated axial pressure gradient for $Re_m = 375$. ——, $\alpha = 7.5$; — —, $\alpha = 10$; – – –, $\alpha = 15$, cycles 1, 2, and 3.

of the pipe, or alternatively the most central part of the core, consisting of fluid moving upstream, whereas the surrounding fluid moves downstream. From figures 4(*a*) and 6(*a*) we conclude that the fluid which moves upstream at the end of the period of reversed axial flow, i.e. at $t = \frac{1}{4}\pi$, occupies a larger portion of the core for larger values of the frequency parameter.

During the decelerative part of the volumetric flow rate, i.e. parts (*d–f*), the axial flow consists of a boundary layer and an inviscid core.

At $t = \frac{1}{4}\pi$, i.e. part (*a*) of figures 4 and 6, the secondary flow consists of a single vortex located inwards. At a time $\frac{1}{4}\pi$ later, i.e. $t = \frac{1}{2}\pi$, figures 4(*b*) and 6(*b*) show that Lyne-type motion (i.e. inward secondary motion at the centre) has occurred for $\alpha = 7.5$, while for $\alpha = 10$ there are signs of inward motion on the outer side of the centre, and at the inner bend. This Lyne-type motion does not last very long. At $t = \frac{3}{4}\pi$, figure 4(*c*) shows that the secondary flow has returned to a Dean-type motion (i.e. one vortex on the half-cross-section) and that it is much stronger than at earlier times. Figure 6(*c*) shows that at higher α the inward motion at the outer bend persists, giving rise to practically two vortices: one on the outer bend and one at $\phi = \frac{1}{2}\pi$. For the remainder of the cycle, i.e. $\pi \leqslant t \leqslant 2\pi$, the secondary flow for $\alpha = 7.5$ consists of one vortex. On the other hand, the secondary flow for $\alpha = 10$ shows a single vortex at $t = \pi$ (figure 6*d*); a multiple-vortex structure at $t = \frac{5}{4}\pi$ (not shown) with a small vortex at the centre and one at the inner bend which persists until $t = \frac{3}{2}\pi$; and a single vortex, once again at the end of the cycle.

The shear-stress plots, figures 5 and 7, show that the circumferential component, $\tau_{r\phi}$, contributes almost as much as two-thirds of the axial component, $\tau_{r\theta}$, to the net shear. These figures also show the location of maximum $\tau_{r\phi}$ oscillating back and forth between the inner and outer bend but with very small amplitude, around $\phi = \frac{1}{2}\pi$.

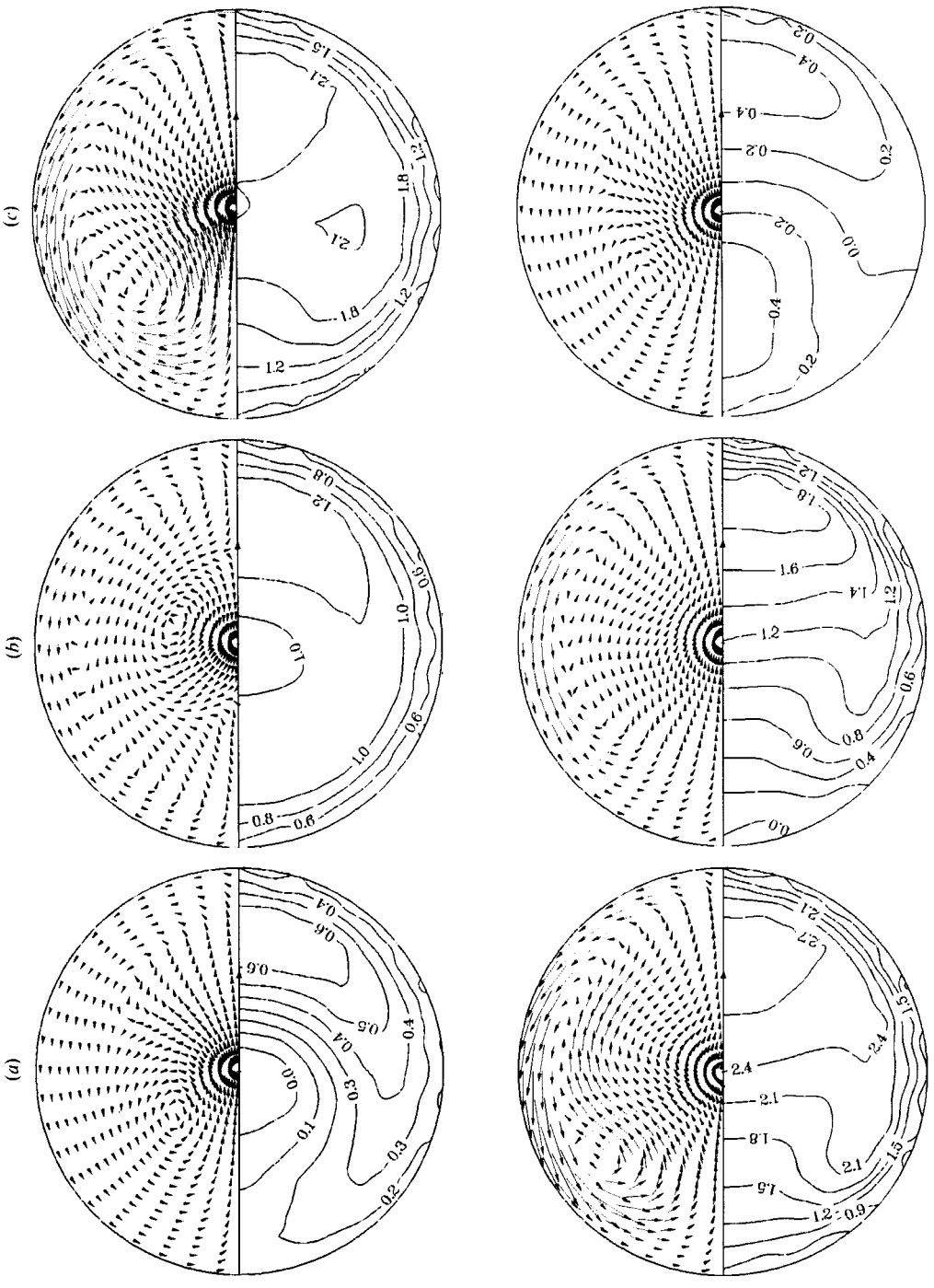

FIGURE 4. Secondary-velocity vectors and axial isovelocity contours for $\alpha = 7.5$, $Re_m = 375$. The centre of curvature of the tube is on the left. Times: (a) $t = \frac{1}{4}\pi$; (b) $\frac{1}{2}\pi$; (c) $\frac{3}{4}\pi$; (d) π; (e) $\frac{3}{2}\pi$; (f) 2π.

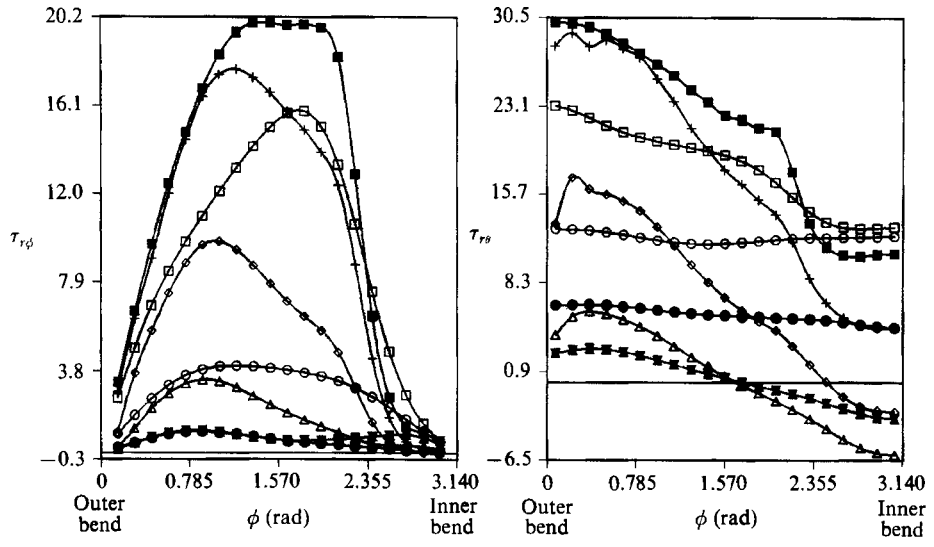

FIGURE 5. Circumferential and axial shear stresses for $\alpha = 7.5$, $Re_m = 375$. Symbols for times plotted: ●, $\frac{1}{4}\pi$; ○, $\frac{1}{2}\pi$; □, $\frac{3}{4}\pi$; ■, π; +, $\frac{5}{4}\pi$; ◇, $\frac{3}{2}\pi$; △, $\frac{7}{4}\pi$; ×, 2π.

Signs of separation of the secondary flow, demonstrated by negative shear, are more dramatic for $\alpha = 10$. One point worthy of note is that whenever such separation is observed, it always occurs at the inner bend. The maximum $\tau_{r\phi}$ occurs in both cases, $\alpha = 7.5$ and $\alpha = 10$, at $t = \pi$, and the minimum at $t = \frac{1}{4}\pi$.

The plots of axial shear stress in figures 5 and 7 show clearly evidence of reverse flow and demonstrate how this region moves more inwardly at lower α. The maximum shear is located at the outer bend and occurs at $t = \pi$.

For $\alpha = 15$ and $315 \leqslant Re_m \leqslant 400$ we find a striking feature – the velocity field varies periodically with time but with a period of three volumetric-flow-rate cycles, i.e. the results for the velocity field exhibit the phenomenon of period tripling. The computed axial pressure gradient, on the other hand, does not exhibit such behaviour, $\partial P/\partial\theta$ varies periodically with time but with period one. As an illustration of this phenomenon of period tripling, we exhibit our results for $\alpha = 15$ and $Re_m = 375$ in figures 8–13. The calculated axial pressure gradient is identical for all three cycles, and shown in figure 3.

At $t = \frac{1}{4}\pi$, figures 8(*a*), 10(*a*) and 12(*a*) show some differences between the three velocity profiles. At this point most differences, with regard to both the secondary and axial velocity fields, are located on the outer half of the cross-section. The inner half consists primarily of a single vortex. At $t = \frac{1}{2}\pi$ we observe some separation of the secondary flow at the inner bend, while most differences still lie on the outer half of the cross-section.

The differences between the three profiles start to become pronounced at $t = \frac{3}{4}\pi$ (figures 8*c*, 10*c*, 12*c*), and afterwards. At $t = \frac{3}{4}\pi$ the secondary flow at the inner and outer bends oscillates between inward and outward flow. This oscillation continues to cover almost the entire centreplane at $t = \pi$. In fact, at this time the secondary flow at the centre oscillates between Lyne-type (figure 8*d*) and outward flow (figure 12*d*). The same oscillations and complex, multiple vortex structures continue for most of the cycle. Though two of the profiles have returned to almost a single vortex located at the inner bend at $t = \frac{7}{4}\pi$ and $t = 2\pi$ (see e.g. figures 10*f* and 12*f*), the profile of the

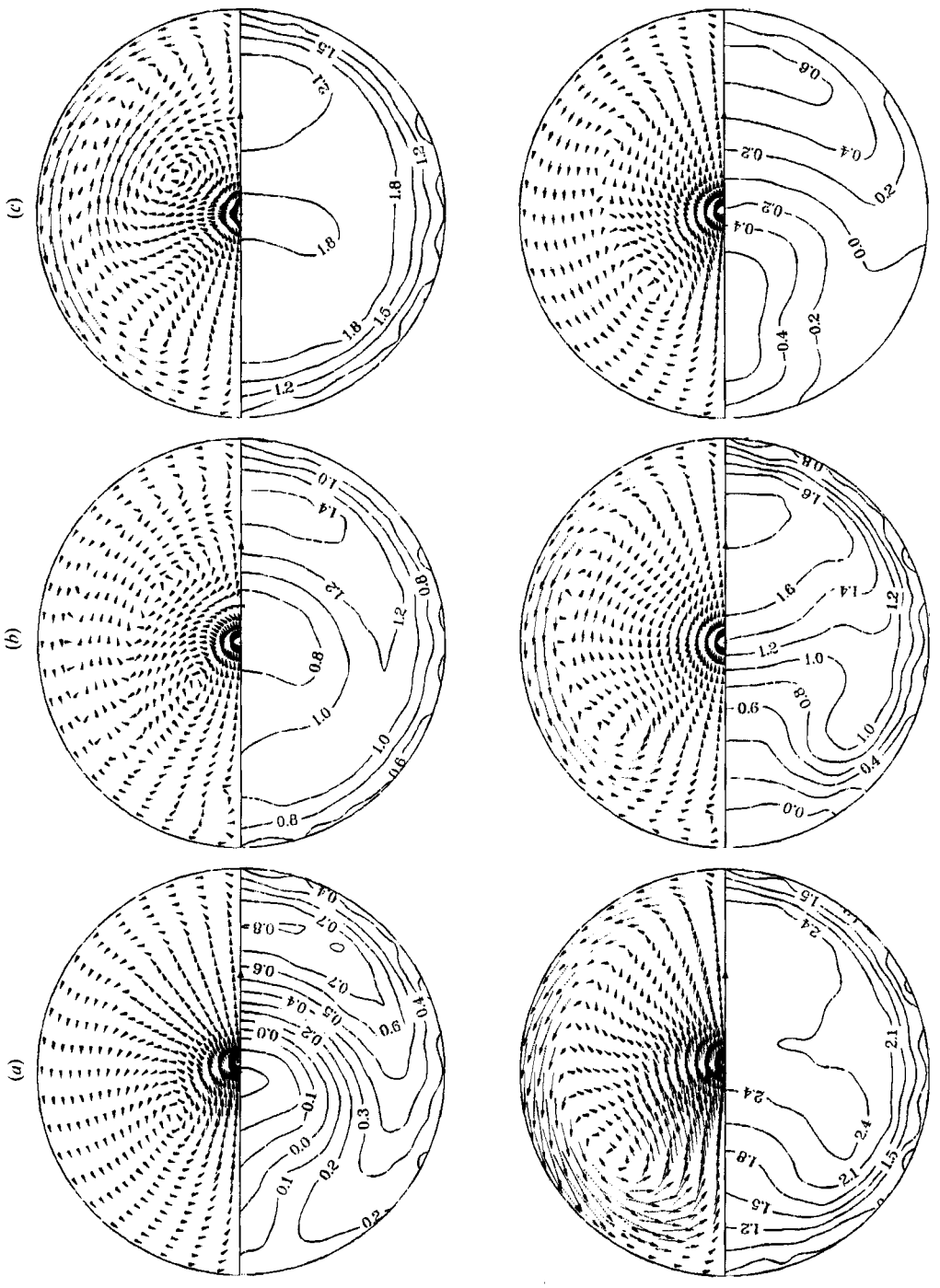

FIGURE 6. Secondary-velocity vectors and axial isovelocity contours for $\alpha = 10$, $Re_m = 375$. The centre of curvature of the tube is on the left. Times: (*a*) $t = \frac{1}{4}\pi$; (*b*) $\frac{1}{2}\pi$; (*c*) $\frac{3}{4}\pi$; (*d*) π; (*e*) $\frac{3}{2}\pi$; (*f*) 2π.

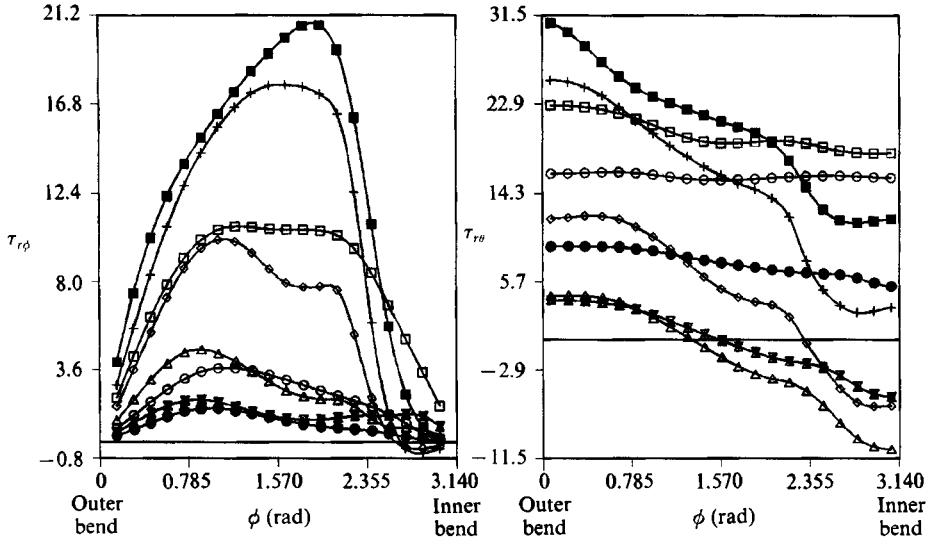

FIGURE 7. Circumferential and axial shear stresses for $\alpha = 10$, $Re_m = 375$. For the legend see figure 5 caption.

first cycle (figure 8*f*) develops into two counter-rotating vortices on the half-cross-section. But at the same time a reversed-flow region has appeared at the inner bend. The combination of these two motions in the three-dimensional space would result in helical motion upstream, in the inner half of the cross-section, and helical motion downstream at the outer half, as is evident from figure 8*f*.

Oscillations can also be observed in the shear-stress curves. Figures 9, 11, and 13 show the circumferential and axial components of shear stress, respectively, for all three cycles. The maximum of $\tau_{r\phi}$ occurs at $t = \frac{5}{4}\pi$ for all three cycles, and the maximum of $\tau_{r\theta}$ at $t = \frac{3}{4}\pi$. This is in contrast to the results for smaller α which showed the maxima of both $\tau_{r\phi}$ and $\tau_{r\theta}$ to occur at $t = \pi$. Another point of interest is the existence of multiple peaks and valleys in the $\tau_{r\phi}$ plots. This is indicative of complex vortical structures with multiple vortices, which is consistent with the flow-field-development figures.

Discussion of a more complete set of results is given in Hamakiotes (1988).

4. Conclusions

The fully developed region of periodic flows through curved tubes has been simulated numerically and the results analysed and discussed. A sinusoidally varying volumetric flow rate was imposed and a solution sought of the flow field consistent with this flow rate. The effects of Reynolds number and frequency parameter have been investigated extensively in the ranges $50 \leqslant Re_m \leqslant 450$ and $7.5 \leqslant \alpha \leqslant 25$. All results were obtained for the values of curvature ratio and amplitude ratio, $\delta = \frac{1}{7}$ and $\gamma = 0.98$, respectively. To check the validity and consistency of our code we have reproduced Gong's (1979) results (the detailed comparisons can be found in Hamakiotes 1988). The agreement is very good. The principal conclusions, drawn primarily from the results presented and described in this paper, can be summarized as follows:

(i) The amplitude of the axial pressure gradient decreases with increasing Reynolds number, and increases with increasing frequency parameter.

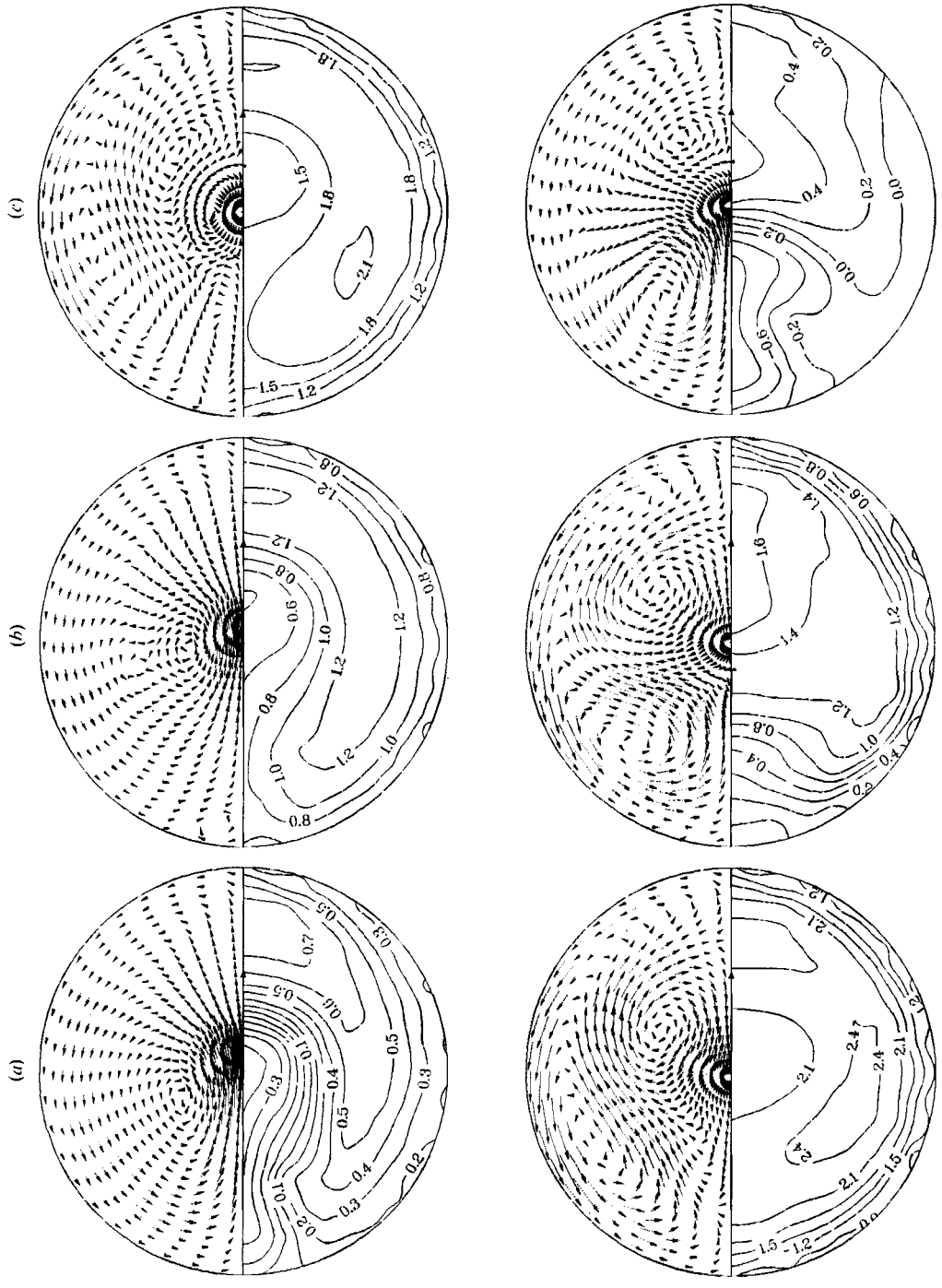

FIGURE 8. Secondary-velocity vectors and axial isovelocity contours for $\alpha = 15$, $Re_m = 375$, cycle 1. The centre of curvature of the tube is on the left. Times: (*a*) $t = \frac{1}{4}\pi$; (*b*) $\frac{1}{2}\pi$; (*c*) $\frac{3}{4}\pi$; (*d*) π; (*e*) $\frac{5}{4}\pi$; (*f*) 2π.

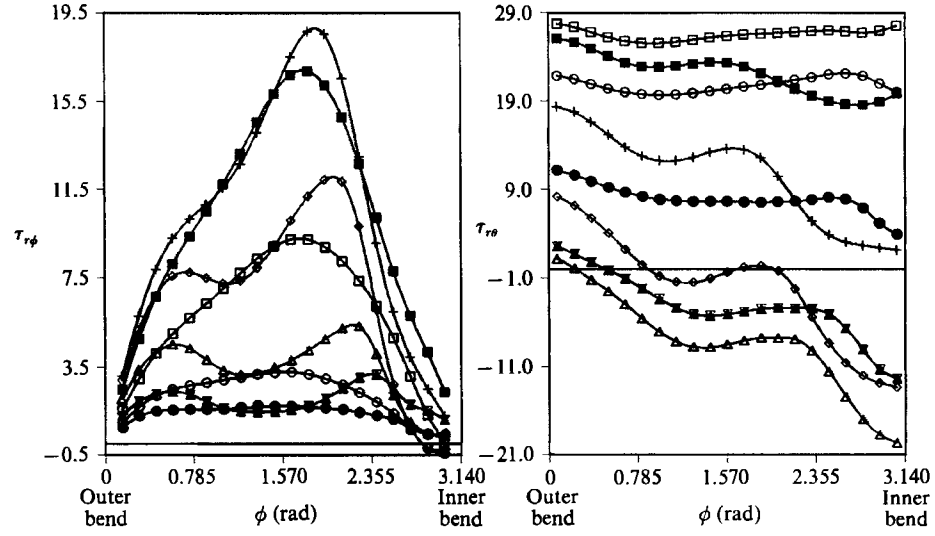

FIGURE 9. Circumferential and axial shear stresses for $\alpha = 15$, $Re_m = 375$, cycle 1. For the legend see figure 5 caption.

(ii) The axial flow is reversed for $\frac{7}{4}\pi \leqslant t \leqslant \frac{9}{4}\pi$. This reversed flow starts at $t = \frac{7}{4}\pi$ and is initiated at the inner bend. It occupies the region of maximum extent at $t = 2\pi$. It is last seen at $t = \frac{9}{4}\pi$ around the centre. At this last time, i.e. at the end of the reversed axial flow duration, there is a portion around the centre which moves upstream (reversed-flow region), while the surrounding fluid moves downstream. This area of reverse axial flow at the core occupies a larger portion of the cross-section for larger values of α.

(iii) During the decelerative portion of the volumetric flow rate the axial flow consists of a boundary layer and an inviscid core.

(iv) Lyne-type motion, i.e. inward flow at the centre, occurs during the accelerative part of the flow rate. It occurs at lower α for higher Re_m, and at earlier times in the cycle for lower α.

(v) The maximum circumferential and axial shears occur at $t = \pi$ for $\alpha = 7.5$ and $\alpha = 10$. For higher α, the maximum $\tau_{r\phi}$ occurs at $t = \frac{5}{4}\pi$, and the maximum $\tau_{r\theta}$ occurs at $t = \frac{3}{4}\pi$.

(vi) Perhaps the most fascinating feature occurs for $\alpha = 15$ and $315 \leqslant Re_m \leqslant 400$: period tripling. The computed axial pressure gradient varies periodically with time for each cycle with period that of the volumetric flow rate. The computed velocity field is found to vary also periodically with time, but with a duration of three cycles, i.e. with a period three times that of $Q(t)$. This feature includes oscillation between inward- and outward-directed secondary flow along the centreplane, complex vortical structures, and oscillation upstream and downstream of parts of the cross-sectional fluid in helical fashion.

The above results are especially important because of the recent studies (Friedman *et al.* 1981; Ku *et al.* 1985) relating arterial wall shear stress to human atherogenesis, in particular, the finding that intimal thickening and plaque formation were most likely to occur in regions where the wall shears were low and oscillated rapidly. There is some evidence (Ku *et al.* 1985) that there may even be a threshold value of shear-stress magnitude for plaque development.

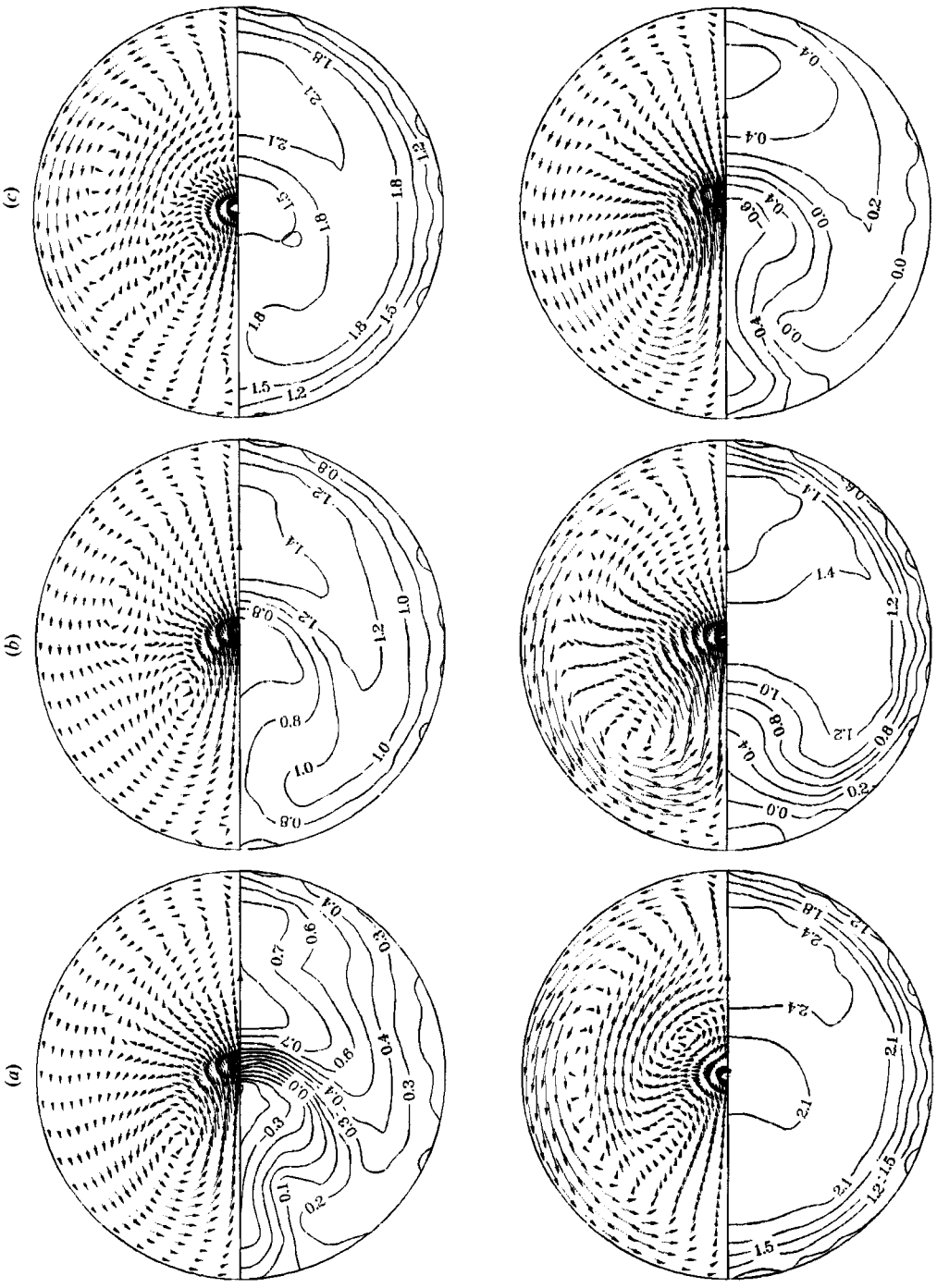

FIGURE 10. Secondary-velocity vectors and axial isovelocity contours for $\alpha = 15$, $Re_m = 375$, cycle 2. The centre of curvature of the tube is on the left. Times: (*a*) $t = \frac{1}{4}\pi$; (*b*) $\frac{1}{2}\pi$; (*c*) $\frac{3}{4}\pi$; (*d*) π; (*e*) $\frac{5}{4}\pi$; (*f*) 2π.

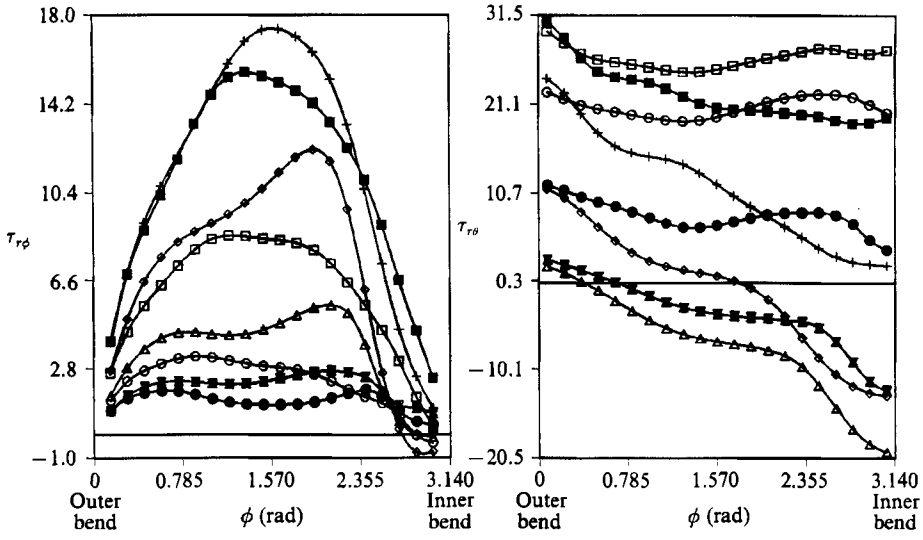

FIGURE 11. Circumferential and axial shear stresses for $\alpha = 15$, $Re_m = 375$, cycle 2. For the legend see figure 5 caption.

A word of caution is in order regarding the assumed symmetry boundary condition. Relatively recent studies by Winters (1984) and Winters & Brindley (1984) suggest caution when imposing this condition because of the existence of asymmetric solutions arising from symmetry-breaking bifurcation points. They also find almost all multiple solutions to be unstable with respect to either symmetric or asymmetric perturbations. But even with the symmetry condition imposed Yang & Keller (1986), Dennis & Ng (1982), and Nandakumar & Masliyah (1982) all report the existence of multiple solutions. It must be pointed out, however, that all aforementioned studies treated only *steady* flows.

In closing, we would like to say a further word on period tripling, and, more generally, the generation in a flow of higher multiples of the basic period. Such effects are known to exist in nonlinear dynamical systems, as has been reported by Feigenbaum, Kadanoff & Shenker (1982), Wersinger, Finn & Ott (1980), José *et al.* (1977), and many others (Guckenheimer & Holmes 1983). Their existence in fluid dynamics has also been confirmed by Libchaber & Maurer (1982) and others. (See, for example, the collection of articles in Cvitanović 1984.) This work has identified a number of routes by which nonlinear systems, in this case fluid flows, undergo transition to chaotic motions, which may be related to transition to turbulence (Gollub & Benson 1980; Lennie *et al.* 1988). One of the most explored of these routes is via period-doubling bifurcations as a controlling parameter takes on increasing values. In addition to 2^n-periods, or cycles, odd-period cycles, beginning with a 3-cycle, have also been observed in fluid mechanical systems (Libchaber & Maurer 1982; Cvitanović 1984). They may be related to 'windows' in period-doubling cascades; these windows are ranges of the controlling parameter for which the system reverts back to a periodic motion from a more 'chaotic' state (Cvitanović 1984). The period-tripling phenomenon uncovered here for a range of Re_m may represent one of these windows.

The existence of the phenomenon of period tripling in our results, along with the studies on multiplicity of solutions mentioned above (although they were all for

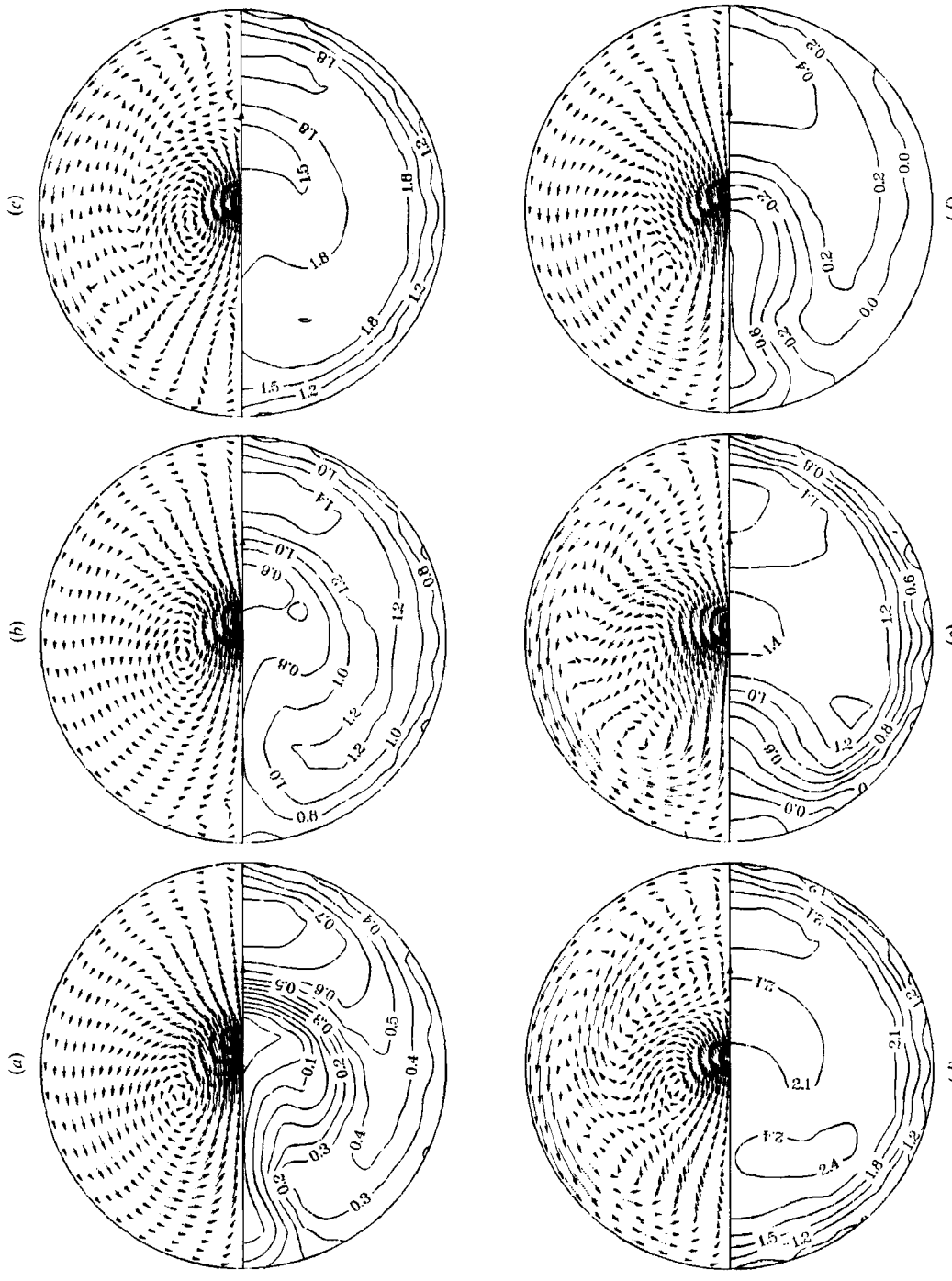

FIGURE 12. Secondary-velocity vectors and axial isovelocity contours for $\alpha = 15$, $Re_m = 375$, cycle 3. The centre of curvature of the tube is on the left. Times: (*a*) $t = \frac{1}{4}\pi$; (*b*) $\frac{1}{2}\pi$; (*c*) $\frac{3}{4}\pi$; (*d*) π; (*e*) $\frac{3}{2}\pi$; (*f*) 2π.

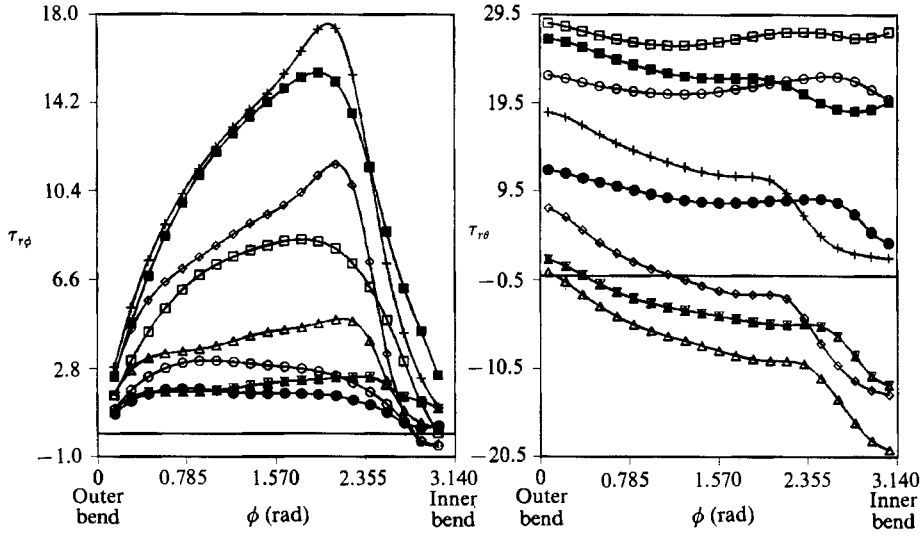

FIGURE 13. Circumferential and axial shear stresses for $\alpha = 15$, $Re_m = 375$, cycle 3. For the legend see figure 5 caption.

steady flows and no direct conclusion can be drawn regarding their existence in unsteady fluid-dynamical systems), provide reason to study unsteady flows in a new light, considering them from the point of view of dynamical systems and their transition to chaos and turbulence. The current state of theoretical understanding and our present results are too incomplete to provide definitive answers to such questions as whether the period tripling found here is the first sign on the road to chaos and transition for unsteady flows through curved pipes. In the meanwhile, it is noteworthy that such flows are capable of period bifurcations which should be discernible by experiment.

The authors wish to acknowledge the support and assistance of Professors Lawrence Talbot and Alexander Chorin of the University of California at Berkeley.

This study was completed under the support of the National Science Foundation under Grant No. MEA-8116360 and ECE-8417852.

REFERENCES

BERGER, S. A., TALBOT, L. & YAO, L.-S. 1983 Flow in curved pipes. *Ann. Rev. Fluid Mech.* **15**, 461.

CARO, C. G., FITZ-GERALD, J. M. & SCHROTER, R. C. 1971 Atheroma and arterial wall shear. Observation, correlation and proposal of a shear dependent mass transfer mechanism for atherogenesis. *Proc. R. Soc. Lond.* B **177**, 109.

CHORIN, A. J. 1968 Numerical solution of the Navier–Stokes equations. *Maths Comput.* **22**, 745.

CVITANOVIĆ, P. (Ed.) 1984 *Universality in Chaos.* Bristol: Adam Hilger.

DEAN, W. R. 1927 Note on the motion of fluid in a curved pipe. *Phil. Mag.* **4**, 208.

DEAN, W. R. 1928 The stream-line motion of fluid in a curved pipe. *Phil. Mag.* **5**, 673.

DENNIS, S. C. R. & NG, M. C. 1982 Dual solution for steady laminar flow through a curved tube. *Q. J. Mech. Appl. Maths* **35**, 305.

FEIGENBAUM, M. J., KADANOFF, L. P. & SHENKER, S. J. 1982 Quasiperiodicity in dissipative systems: A renormalization group analysis. *Physica* **5D**, 370.

FRIEDMAN, M. H., HUTCHINS, G. M., BARGERON, C. B., DETERS, O. J. & MARK, F. M. 1981 Correlation between intimal thickness and fluid shear in human arteries. *Atherosclerosis* **39**, 425.

FRY, D. L. 1968 Acute vascular endothelial changes associated with increased blood velocity gradients. *Circul. Res.* **22**, 165.

FRY, D. L. 1973 Responses of the arterial wall to certain physical factors. In *Atherogenesis: Initiating Factors*. Ciba Symposium vol. 12, p. 93. North-Holland: Elsevier. Excerpta Medica.

GOLLUB, J. P. & BENSON, S. V. 1980 Many routes to turbulent convection. *J. Fluid Mech.* **100**, 449.

GONG, K. O. 1979 Experimental study of unsteady entrance flow in a curved pipe. Ph.D. thesis. University of California, Berkeley.

GUCKENHEIMER, J. & HOLMES, P. 1983 *Nonlinear Oscillations, Dynamical Systems, and Bifurcations of Vector Fields*. Springer.

HAMAKIOTES, C. C. 1988 Periodic flows through curved tubes. Ph.D. thesis. University of California, Berkeley.

HAMAKIOTES, C. C. & BERGER, S. A. 1988 Fully developed pulsatile flow in a curved pipe. *J. Fluid Mech.* **195**, 23.

ITŌ, H. 1987 Flow in curved pipes. *JSME Intl J.* **30**, 543.

JOSÉ, J. V., KADANOFF, L. P., KIRKPATRICK, S. & NELSON, D. R. 1977 Renormalization, vortices, and symmetry-breaking perturbations in the two-dimensional planar model. *Phys. Rev.* B **16**, 1217.

KU, D. N., GIDDENS, D. P., ZARINS, C. K. & GLAGOV, S. 1985 Pulsatile flow and atherosclerosis in the human carotid bifurcation. *Arteriosclerosis* **5**, 293.

LENNIE, T. B., MCKENZIE, D. P., MOORE, D. R. & WEISS, N. O. 1988 The breakdown of steady convection. *J. Fluid Mech.* **188**, 47.

LIBCHABER, A. & MAURER, J. 1982 A Rayleigh Bénard experiment: helium in a small box. In *Nonlinear Phenomena at Phase Transitions and Instabilities* (ed. T. Riste), p. 259. Plenum.

LYNE, W. H. 1971 Unsteady viscous flow in a curved pipe. *J. Fluid Mech.* **45**, 13.

NANDAKUMAR, K. & MASLIYAH, J. H. 1982 Bifurcation in steady laminar flow through curved tubes. *J. Fluid Mech.* **119**, 475.

NANDAKUMAR, K. & MASLIYAH, J. H. 1986 Swirling flow and heat transfer in coiled and twisted pipes. In *Advances in Transport Processes*, vol. 4 (ed. A. S. Mujumdar and R. A. Masliyah). Wiley Eastern.

NEREM, R. 1981 Arterial fluid dynamics and interactions with the vessel walls. In *Structure and Function of the Circulation*, vol. 2 (ed. C. J. Schwartz, N. T. Werthessen & S. Wolf). Plenum.

SCHETTLER, G. *et al.* (Eds.) 1983 *Fluid Dynamics as a Localizing Factor for Atherosclerosis*. Springer.

WERSINGER, J.-M., FINN, J. M. & OTT, E. 1980 Bifurcation and "strange" behavior in instability saturation by nonlinear three-wave mode coupling. *Phys. Fluids* **23**, 1142.

WINTERS, K. H. 1984 A bifurcation study of laminar flow in a curved tube of rectangular cross-section. *Harwell Rep.* AERE-TP, 1104.

WINTERS, K. H. & BRINDLEY, R. C. G. 1984 Multiple solutions for laminar flow in helically-coiled tubes. *Harwell Rep.* AERE-R, 11373.

YANG, Z. & KELLER, H. B. 1986 Multiple laminar flows through curved pipes. *Appl. Numer. Maths* **2**, 257.